Experiments in Fluids (2026) 67:65
https://doi.org/10.1007/s00348-026-04225-y

RESEARCH ARTICLE

# On the accuracy of multi-exposure 3D-PTV

**A. Grille Guerra[1] · B. Wieneke[2] · F. Scarano[1]**

Received: 22 January 2026 / Revised: 26 March 2026 / Accepted: 16 April 2026


**Abstract**

Multi-exposure (ME) 3D particle tracking velocimetry (3D-PTV) is a specific recording variant whereby more than two samples of the particle position are obtained to overcome some limitations of single-exposure double-frame recordings, such as accelerometry, pressure from PIV, or to further extend the dynamic velocity range. Compared to time-resolved (TR) systems, ME lowers system requirements in terms of laser power and camera frame rate. Although proved viable only recently using asymmetric timing sequences, a systematic assessment of ME 3D-PTV robustness and accuracy that covers both single-frame and double-frame recording is missing, which is the aim of the present work. The reliability and accuracy of particle tracking in ME recordings comprising up to 5 exposures with one or two frames are first scrutinized on a synthetic particle field motion based on a Taylor–Green vortex lattice. Single-frame ME yields viable results, with a detection rate of 90% up to a cumulated particle image density of 10% (cppp = 0.1). The error rate, however, remains below 5% only when the exposures are distributed over two frames. The measurement accuracy in terms of dynamic velocity and acceleration ranges is reported, as a function of particle image density, number of pulses and timing sequence. The results suggest approximate equivalence to the time-resolved systems in terms of dynamic velocity range (DVR). The dynamic acceleration range (DAR) instead only approaches that of time-resolved analysis for specific combinations of number of pulses and sequence timing. ME recordings are simulated from a time-resolved experiment around a wall-mounted cube, which yield equivalence between ME (4 pulses distributed onto 2 frames) and TR conditions. A demonstration of ME 3D-PTV for accelerometry and pressure from PIV is obtained, with experiments in the turbulent wake of a circular cylinder.

## 1 Introduction

Three-dimensional Lagrangian particle tracking (LPT, Schröder and Schanz 2023) represents nowadays the state of the art for the detailed inspection of 3D flows. Initial efforts to realize 3D-PTV measurements (Nishino et al. 1989; Maas et al. 1993; Malik et al. 1993) have set the foundations of volumetric imaging, particle image detection, triangulation and pairing, to render the velocity field at the sparse locations of the tracers. These methods evolved toward algorithms using advanced Lagrangian predictor–corrector schemes for particle pairing (Willneff 2003), the iterative particle reconstruction (IPR, Wieneke 2013) and most notably the shake-the-box method (STB, Schanz et al. 2016). The latter combines IPR with an advanced Lagrangian initialization of the particle field, largely reducing the complexity of particle images triangulation. As a result, STB is currently utilized in several 3D experiments to deal with a number of trajectories in excess of 100,000/Mpx (ppp = 0.1) as recently surveyed (Schröder and Schanz 2023). These conditions enable dense (gridded) reconstruction of the velocity field and its gradient and under some conditions, of the fluid flow pressure distribution. Experiments rely on the use of high-speed illuminators coupled with high-frame-rate cameras to finely describe the tracers' motion along their trajectories. The latter requires a small time separation $\Delta t_0$ and a fine displacement, compared to the inter-particle distance. The corresponding system requires a relatively high repetition rate, $f = 1/\Delta t_0$ as illustrated in Fig. 1a. The most practiced recording mode in PIV and PTV is the double-frame, based on two separate laser cavities fired at an arbitrary delay and an imager capable to acquire two frames with temporal separation as low as a microsecond. This mode of operation is particularly useful in high-speed flows (e.g., in the compressible regime), otherwise requiring systems repetition rate in the order of 100 kHz, unless dedicated burst illumination and imagers are adopted (Beresh et al.

✉ A. Grille Guerra
a.grilleguerra@tudelft.nl

[1] Aerospace Engineering, TU Delft, Delft, The Netherlands

[2] LaVision GmbH, Göttingen, Germany

Published online: 16 May 2026

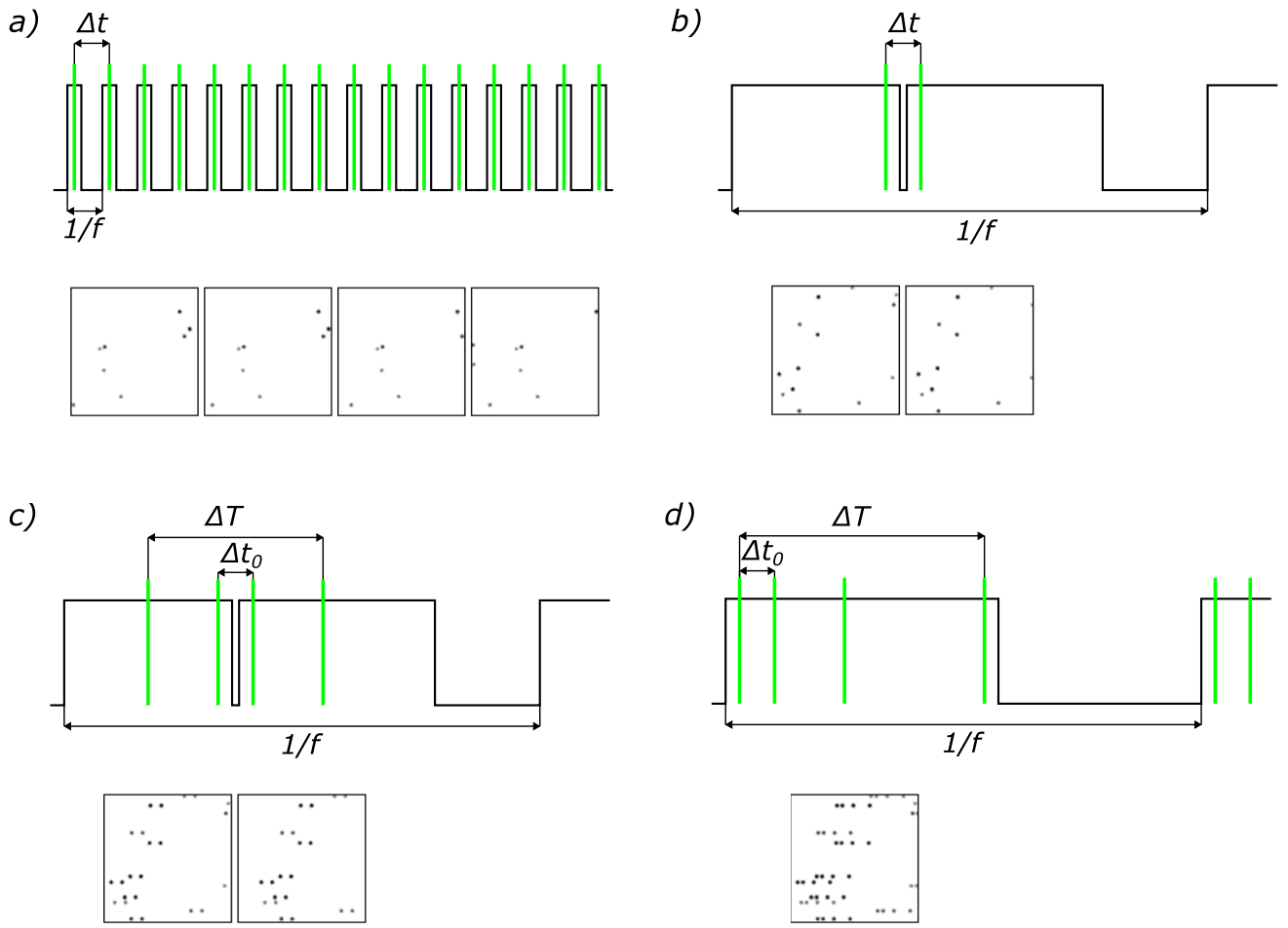


**Fig. 1** Template of illumination pulses and camera exposure, with corresponding image details, for time-resolved mode (**a**), double frame with two (**b**) and four pulses (**c**); single frame with four pulses (**d**)

2015; Thurow et al. 2013). The above considerations apply to planar PIV, PTV as well as to volumetric 3D measurements. Volumetric double-frame recording has been largely practiced for PTV in aerodynamic flows (Saredi et al. 2020), where the measurement conditions (flow velocity, optical magnification, seeding density) do not allow time-resolved recording (Novara et al. 2016, 2023). Figure 1b illustrates the timing diagram of illumination and image acquisition for the double-frame recording mode, featuring light pulses around the transition between the two frames. Volumetric measurements around complex objects require multiple, redundant views for volume coverage (Hysa et al. 2024). The latter problem has been largely simplified by the introduction of object-aware particle reconstruction and tracking (Wieneke and Rockstroh 2024) along with the necessary object registration techniques (Hendriksen et al. 2024). As a result, the number of cameras in an experiment has upscaled from the typical set of 4 used in tomographic PIV (Elsinga et al. 2006) to 8 or 12 (Hendriksen et al. 2024). In the latter conditions, it may be argued that the adoption of low-repetition-rate systems is a more viable option, compared to kilohertz rate imagers, based on data rate, data requirement for statistical convergence and overall system specifications and complexity.

Despite the versatility of the double-frame recording technique, velocity measurements based on only two pulses suffer from an intrinsic compromise between the random and truncation errors (Boillot & Prasad 1996), in turn limiting the measurement dynamic velocity range (DVR, Adrian 1997). Varying the time separation also affects measurement robustness in PTV (particle pairing success rate) as well as the signal-to-noise ratio (SNR) of cross-correlation analysis. The compromise is mitigated by adding more samples of the particle position along its trajectory, which is practiced with multi-exposure (ME) techniques discussed in the following.

Multi-exposure (ME) timing strategies with 3 or more illumination pulses offer the possibility of increasing the dynamic range of the measurement over two-pulse double-frame systems, while providing acceleration estimation, relevant for data assimilation strategies (Godbersen et al. 2024;

Schneiders and Scarano 2016) involving pressure estimation. The analysis of ME recordings has long stood as a challenging problem, especially for single-frame systems, due to the directional ambiguity of the particle traces (Adrian, 1991; Adrian and Westerweel 2011). For double-frame recordings, as shown in Fig. 1c, a four-pulse strategy has been proposed by Novara et al. (2019) within the STB framework, using the time information across the two frames to solve said ambiguity. Multi-exposure single-frame recordings would further simplify the hardware requirements and system synchronization. The problem has been attempted recently by streak analysis (Zhang et al. 2024) or in the early work of Agüí and Jiménez (1987), who made use of a dot–streak–dot combination. A recent solution has been proposed that makes use of asymmetric timing templates, as shown in Fig. 1d, which disambiguate the direction of motion using kinematic similarity as a detection criterion (Scarano et al. 2025).

Although the viability of ME PTV based on asymmetric time sequences has been shown, measurement accuracy and robustness depend upon several parameters, such as the sequence timing template and its length, the particle image density and the use of one or two frames to record the template. Furthermore, evidence of an increased dynamic velocity and acceleration range has only been hypothesized and a conclusive study is needed to determine whether ME 3D-PTV can surrogate the time-resolved STB technique. Therefore, the present study examines the tracking accuracy of ME recordings in the context of 3D-PTV. A tracking algorithm is described that deals with arbitrary timing templates for both single- and double-frame recordings. The working principle is first illustrated using numerically generated images from imposed particles' motion. The principles are verified on ME 3D-PTV data simulated from an experiment conducted in time-resolved mode, which yields a quantitative analysis of performance under more realistic conditions. Finally, an experimental demonstration is conducted, for completeness, which illustrates the viability of 3D pressure from ME 3D-PTV.

## 2 Generalized ME tracking algorithm

A multi-exposure (ME) sequence consists of particles illuminated by $N$ pulses. The discussion is generalized here to the case where such $N$ pulses are captured onto a single-frame or a double-frame recording. The pulses are taken at times $t_1, t_2, \dots, t_N$, with corresponding time separation $\Delta t_1, \dots, \Delta t_{N-1}$. For simplicity, the time separation is normalized with respect to the smallest time separation, $\Delta t_0$, in the shape $\Delta t^* = \frac{\Delta t_1}{\Delta t_0}, \dots, \frac{\Delta t_{N-1}}{\Delta t_0}$, where $\Delta t_0$ typically corresponds to a displacement of 5–10 pixels in the camera images. For every particle trajectory, a trace of $N$ dots is formed, at the corresponding particle locations $\boldsymbol{x}_1, \boldsymbol{x}_2, \dots, \boldsymbol{x}_N$. The sequence is characterized by the number of pulses in each frame and the chosen timing template. A specific notation is introduced for compactness in the remainder, whereby the number of frames, exposures and relative time intervals are indicated. For example, ME(1 + 2, $\Delta t^*$=1–2) refers to a double-frame recording (denoted by the + symbol) with one pulse in the first frame and two in the second (1 + 2), with non-uniform time separation ($\Delta t_1 = \Delta t_0$ and $\Delta t_2 = 2\Delta t_0$, thus $\Delta t^*$=1–2). Similarly, ME(4, $\Delta t^*$=1–2-3) corresponds to a single-frame recording that captures four pulses with non-uniform separation in proportion to 1, 2 and 3. Such asymmetric distribution is necessary to resolve the directional ambiguity, as discussed in Scarano et al. (2025).

A sketch of the particle tracking process is shown in Fig. 2. The algorithm involves a double-iterative exercise of 3D particle reconstruction. The inner loop is based on the IPR approach (Wieneke 2013; Jahn et al. 2021). Once the first 3D distribution of particle samples is obtained, particle samples need to be associated to a trajectory (tracking step) yielding the traces ascribing a time tag and a trajectory tag to each sample. Such a process may differ depending on whether the single- or double-frame recording approach is taken. However, many aspects of the method remain similar, and the remainder describes the general aspects of it.

Trace detection in time-resolved particle tracking (e.g., shake-the-box) is based on the (marching) process that extrapolates an existing trajectory toward the expected occurrence of the next particle sample. For double-frame single-exposure analysis, trace detection reduces to the problem of particle pairing, often based on the nearest neighbor principle. The latter can be stabilized by imposing a condition based on the spatial regularity of the velocity. The criterion of minimum dispersion of the velocity from a group of pairs has been widely used in 3D-PTV in various ways as also been proved effective in a recent work (Le Bris et al. 2025).

In the present approach, ME recordings are used to generate candidate traces (Sect. 2.1) followed by a selection procedure that identifies the most likely trace, based on minimization of a cost function (Sect. 2.2). The following sections detail such a process of trace detection.

### 2.1 Trace candidates generation

From the volumetric particle distributions obtained with 3D particle reconstruction, the search for candidate traces is performed in a chosen neighborhood of a selected sample. The procedure is exemplified considering a ME(3, $\Delta t^*$ = 1–2) recording. The neighborhood comprises three (not yet detected) traces, each made of three exposures (Fig. 3(a)).

The search for the trace including the selected sample $P_\mathrm{i}$ (in green in Fig. 3) requires assuming the reference time $t_{ref}$

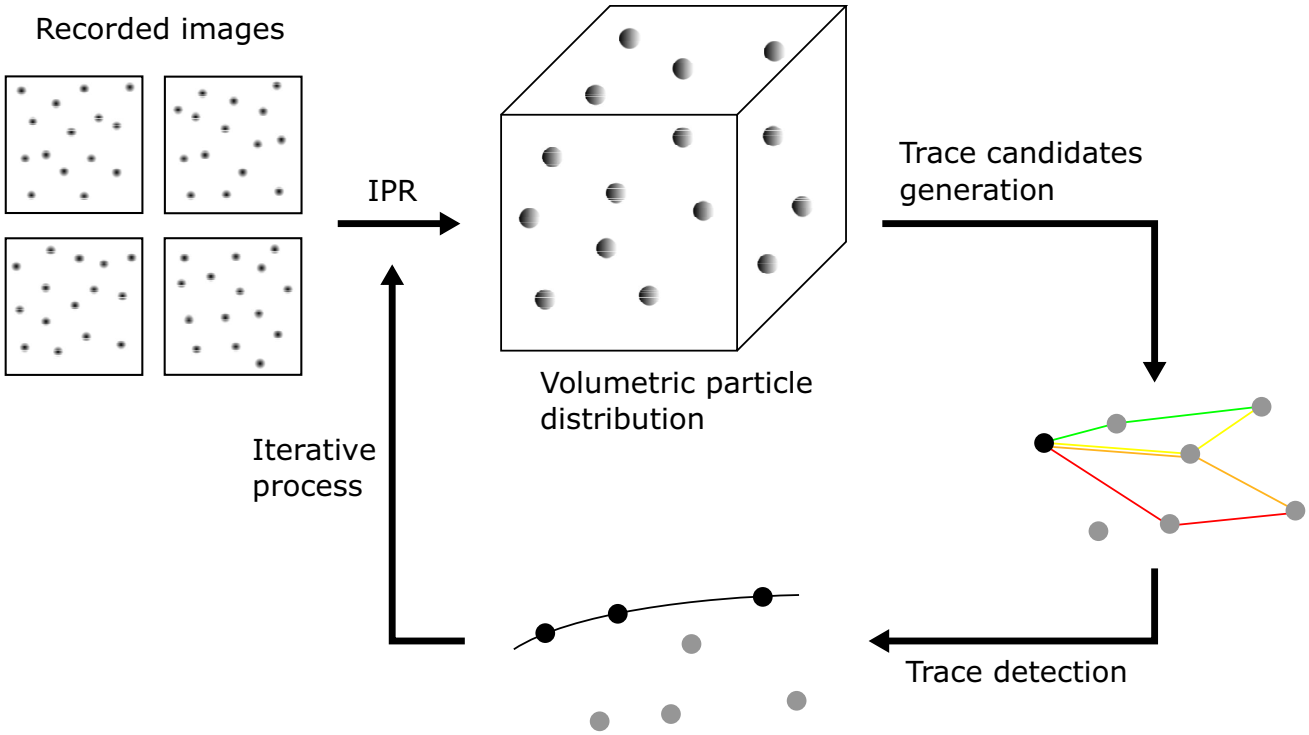


**Fig. 2** Schematic description of the iterative particle detection and tracking for ME-STB. Single-frame images are recorded from a four-camera system; 3D particle positions are obtained with IPR; groups of particles complying with the kinematic likelihood are candidate traces; cost function minimization identifies the physical traces. The latter are iteratively fed into IPR to confirm or discard particles from the previous distribution

of the sample. Without lack of generality, one can assume $t_{ref} = t_1$ in the present example. For a specified velocity range, $\boldsymbol{v}_{range}$ (Fig. 3(b)) particle matches are searched in the neighborhood of $P_i$. In general, the search region may be a sphere or a cuboid, but the use of a velocity predictor (Novara et al. 2023) may significantly accelerate the search by reducing the spatial extent where candidate matches are sought for.

For every matched pair, the search continues forward, collecting samples until the trace includes $N$ samples (3 in the present case). After the first match, further branching is informed by the velocity estimated from the initial pair, assuming constant velocity (dashed lines in Fig. 3I). Correspondences are established allowing a departure from the linear extrapolation assuming an acceleration-related range, $a_{range}$, to establish the search radius (Fig. 3(c)). This process is repeated for every particle in the neighborhood, forming a collection of candidate traces (Fig. 3(d)). Since the time correspondences of the particles are unknown, particles not belonging to $t_{ref}$ may result in the generation of wrong traces, as the one depicted in Fig. 3d.

For double-frame recordings, it is advisable to design the sequence with the shortest time separation across the two frames. Thus, $t_{ref}$ pertains to the last pulse of the first frame and $t_{ref+1}$ the first in the second frame, which reduces the number of possible matches and accelerates the detection. For single-frame recordings, instead, the algorithm should begin with the largest $\Delta t_i$. Although this option produces a larger amount of pairs, the probability of overlapping particle images (at low velocity) is minimized.

## 2.2 Trace detection

For each candidate trace, a score is assigned based on the kinematic similarity criterion (Scarano et al. 2025). Furthermore, neighborhood consistency is quantified, according to Wieneke and Rockstroh (2024). A final cost function, $w$, is assigned as the product of both elements, and the best option (lowest $w$) is extracted as the valid trace for the particle. The procedure is exemplified in Fig. 4 for the set of trace candidates generated in Fig. 3.

The kinematic similarity criterion is evaluated along the trace. For each of the $N-1$ segments forming a trace of $N$ pulses, a velocity vector $\boldsymbol{v} = \left(v_x, v_y, v_z\right)$ is obtained from the two particles forming the segment and the time separation between them. Then, a kinematic cost function $w_k$ is constructed for the trace by adding up the standard deviations of the three velocity components, evaluated over the $N-1$ segments:

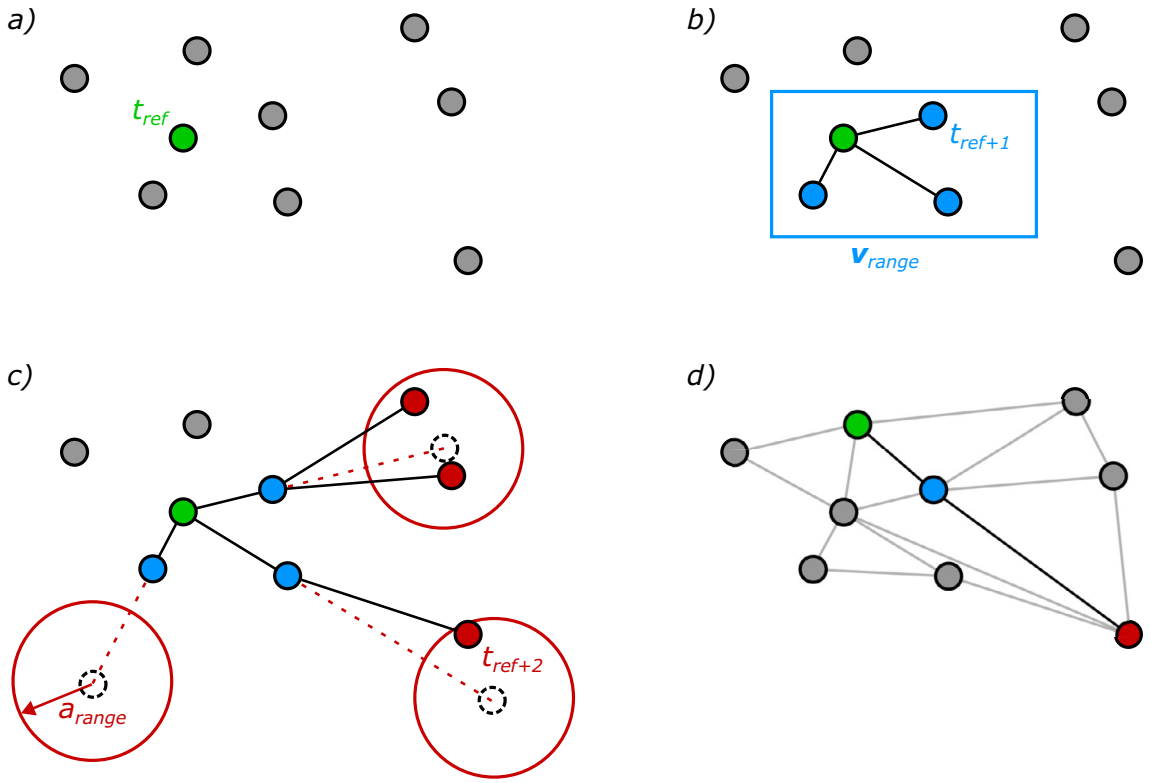


**Fig. 3** Generation of candidate traces for a ME(3, $\Delta t^* = 1$–2) recording. Neighborhood around a selected particle sample (green) at $t_{ref} = t_1$ **a**; matching pairs based at $t_{ref+1}$ within the allowed velocity range, $\boldsymbol{v}_{range}$ **b**; extrapolated trajectories based on estimated velocity and bounded acceleration, $a_{range}$ **c**. Formation of a wrong trace from a particle not belonging to $t_{ref}$ **d**, together with all candidate traces formed

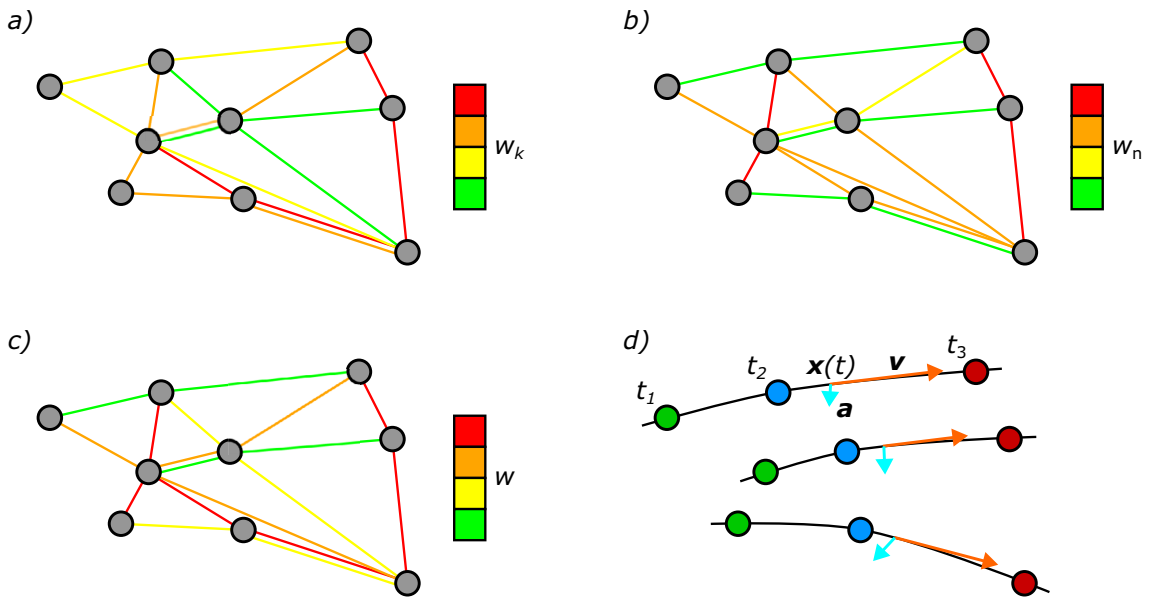


**Fig. 4** Trace detection for an ME(3, $\Delta t^* = 1$–2) situation. Each candidate trace is assigned a score based on kinematic similarity ($w_k$) **a** and neighborhood consistency ($w_n$) **b**, yielding the final cost function ($w$) **c**. Traces with the lowest values of $w$ are accepted. A polynomial function models position, velocity and acceleration at time $t = (t_1 + t_3)/2$ for valid traces **d**

$$w_k = \sigma(v_x) + \sigma(v_y) + \sigma(v_z) \tag{1}$$

The neighborhood consistency expresses the velocity similarity among candidate traces in a limited region of space. For every trace candidate $Tr_i$, the velocity difference with respect to neighboring traces $Tr_k$, $\delta_{i,k}$, is evaluated taking the average over all segments of the trace:

$$\delta_{i,k} = \left\| \overline{\boldsymbol{v}(Tr_i) - \boldsymbol{v}(Tr_k)} \right\| \tag{2}$$

Neighbor traces involving particles shared with $Tr_i$ are not considered, since most likely either $Tr_i$ or those neighbors are ghost traces. For every particle $P_j$ in the neighborhood of $Tr_i$, the best matching trace involving that particle is taken as the most likely correspondence, i.e., $\delta^*_{i,j} = \min(\delta_{i,k})$ between the $k$ traces passing through $P_j$. Finally, a neighborhood cost function $w_n$ (Fig. 4(b)) is constructed as the average of a few ($M$, e.g., 5) best fitting correspondences:

$$w_n(Tr_i) = \frac{\sum_{j=1}^{M} \delta^*_{i,j}}{M} \tag{3}$$

The likelihood of a candidate trace to correspond to a physical trajectory is expressed as the product of the above criteria, $w = w_k \cdot w_n$. Among the set of candidate traces, that exhibiting the lowest value of $w$ is selected as a valid trace for the particle, as shown in Fig. 4c by the green traces.

In the work of Scarano et al. (2025), the particle samples in a given neighborhood are interrogated according to a combinatorial algorithm that varies the time index of the candidate sequence. The kinematic similarity criterion and trace regularity criterion produce respective residuals and their product is considered as a composite criterion for trace detection. Although effective, the approach has two shortcomings: The amount of computations in the combinatorial approach increases rapidly with the number of particles considered in the neighborhood; and the kinematic similarity penalizes tangential acceleration and trace regularity the acceleration magnitude along the trace.

The present approach advances the above by preselecting traces candidates based on regularity, which largely reduces the combinatorial basis for kinematic similarity evaluation, as illustrated in Fig. 3. The second advancement replaces the trace regularity criterion (individual regularity) with that of neighborhood consistency (group regularity), whereby the absolute value of acceleration is not penalized, but rather the spatial variation thereof. Such concept is illustrated in Fig. 4 using the set of trace candidates generated in Fig. 3.

The assignment of particles to traces follows a hierarchical approach: Particle samples ascribed to more than one candidate trace are assigned to the trace with the lowest cost function. After a trace has been accepted, the particle samples are included as the initial distribution for the iterative particle reconstruction (IPR) process (Fig. 2), with the objective of improving the accuracy of particle detection and reducing the amount of spurious detections (ghost particles).

Upon convergence, a second-order polynomial is used to fit the final set of traces. Position, velocity and acceleration are estimated at the intermediate time $t = \frac{t_1 + t_N}{2}$ (Fig. 4(d)).

## 3 Performance analysis

A dataset is produced from an analytical flow field, and a synthetically generated particle distribution is considered here with a flow field described by a steady Taylor–Green vortex lattice, as shown below:

$$\begin{cases} u = u_0 \cos\left(\frac{2\pi x}{\lambda}\right) \sin\left(\frac{2\pi y}{\lambda}\right) \\ v = -u_0 \sin\left(\frac{2\pi x}{\lambda}\right) \cos\left(\frac{2\pi y}{\lambda}\right) \\ w = u_0 \end{cases} \tag{4}$$

where $x$, $y$ and $z$ are the Cartesian coordinates, $u_0 = 5$ m/s is the velocity amplitude of the waves and $\lambda = 800$ mm is their wavelength. Sine-based velocity distributions are a popular choice for numerical assessments (Kähler et al. 2016), focusing the attention on the modulation of the peak value. The present analysis considers a simulated domain of $800 \times 800 \text{x} 200$ mm$^3$. The spatial distribution of the horizontal velocity component is shown in Fig. 5(left).

The $w$-component is set here to a constant value, such that all particles feature a nonzero velocity and the condition of overlapping particle images is avoided for the case of multiple exposures in a single frame. The topic of how to deal with small-to-vanishing velocities—and thus overlapping particle images—remains an open challenge in ME particle tracking, as also discussed in Scarano et al. (2025). Some strategies to overcome this situation are explored in Appendix.

### 3.1 Image generation and ME-STB parameters

The domain of interest is imaged by four cameras with $800 \times 800$ px resolution under simplified conditions of parallel viewing, in-focus imaging and absence of optical distortions. The angle between cameras is 30 °. Tracer particles are rendered with a constant diameter of 2 px and a peak intensity of 700 ±300 counts. The seeding density is described in terms of particles per pixel (ppp), referring to that obtained from a single exposure. The relation between the single-exposure seeding density and the cumulative value from $N$ exposures is cppp = $N \cdot$ ppp. The reference time separation between exposures, $\Delta t_0$, corresponds to particle displacement of 5 px.

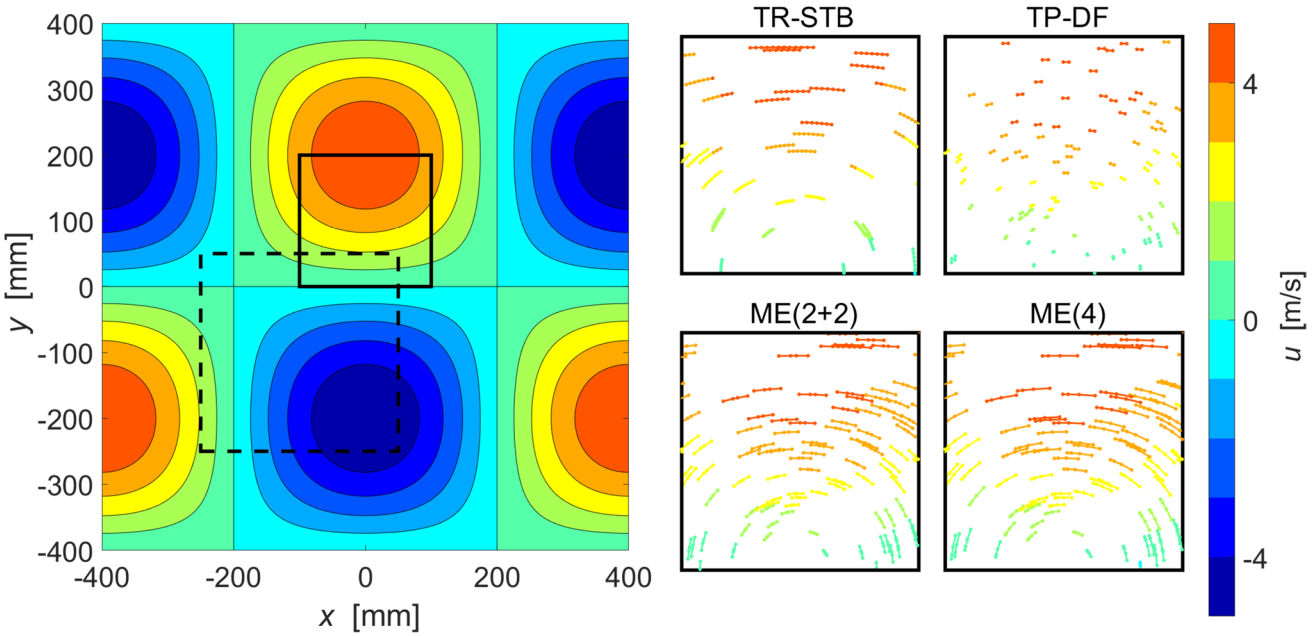


**Fig. 5** Horizontal component of the velocity field (left) and particle traces collected inside the solid black box using various 3D-PTV strategies (right). The dashed black box represents the domain studied in Appendix for the vanishing velocity scenario

Various pulse sequencing strategies have been considered to explore the effect of relevant experimental parameters such as the cumulative seeding density cppp, timing template $\Delta t_i$ and number of exposures $N$. State-of-the-art 3D-PTV methods are considered for reference, namely: time-resolved shake-the-box (TR-STB), two-pulse double-frame STB (TP-DF, Novara et al. 2023) and four-pulse double-frame STB (ME(2 + 2), with $\Delta t^* = 2$–1-2, Novara et al. 2019). Particle traces obtained with the aforementioned methods are shown in Fig. 5(right) alongside the case of four-pulse single-frame recording with an asymmetric time sequence.

A total of 20 passes of the iterative ME-STB procedure (see Fig. 2) are considered, which is sufficient to achieve converged results for all cases included in this section. The velocity and acceleration-related search radii are set globally, based on the maximum values expected from the ground-truth solution. The IPR parameters follow the discussion by Jahn et al. (2021), consisting of 20 and 10 outer and inner loops, respectively, with a linearly increasing triangulation error from 0.25 px up to 1 px.

### 3.2 Seeding density

The accuracy and reliability of ME-STB are examined by varying the concentration of tracer particles (ppp). A correct trace detection is considered when all particle samples comprised in the trace correspond to their exact locations within 1 voxel deviation. To study the influence of seeding density, a recording of type ME(3, $\Delta t^* = 1$–2) is considered. The correct detection rate is given in Fig. 6(left) when the seeding density is varied from sparse (ppp < 0.01) to dense (ppp = 0.05). It should be retained in mind that the corresponding cumulative seeding density cppp approaches 0.15 for the dense conditions. The fraction of correctly detected traces is relatively flat at a level above 90% up to ppp = 0.04. In the same range, the error rate remains below 2%. Beyond ppp = 0.04, a large drop of detected traces and an explosive increase of erroneous traces are observed. This behavior is ascribed to the increased number of faulty particle detections during the particle reconstruction process (IPR) with fewer detected true particles, and the results are in line with the those reported by Jahn et al. (2021). To confirm this hypothesis, additional tests have considered the analysis of the tracking part of the algorithm only, replacing IPR by directly feeding the ground-truth particle positions into the tracking algorithm. In these, the percentage of correct traces has been found to exceed 99% even for cppp levels in the order of 0.3, thus confirming the reliability and robustness of the proposed tracking algorithm.

For the correctly detected traces, the positional accuracy of the detected particles will in turn determine that of the velocity measurement. The normalized histogram of the velocity error—setting the histogram curve to 1 at zero error—is shown in Fig. 6(right) at four selected values of ppp. For mild density (ppp < 0.02), the error stays below 0.5%. Again, the rapid increase beyond ppp ~ 0.04 (cppp ~ 0.12) is ascribed to more ghost particles, which

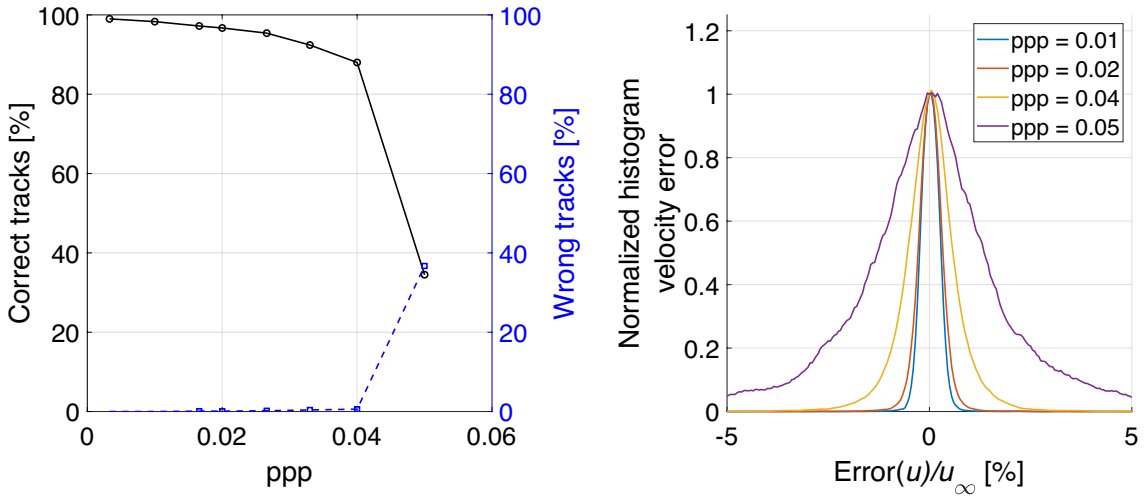


**Fig. 6** Robustness and accuracy of ME-STB, for $N=3$. Percentage of correct and incorrect traces as a function of seeding density (left) and normalized histogram of velocity error (right)

have a strong influence in the final accuracy of the tracking algorithm.

Note that for an ME(3) sequence, if IPR successfully reconstructed 80% of the particles, the maximum expected number of traces would be $0.8^3 \approx 50\%$ only, with a cubic dependence of trace detection rate on the IPR particle detection rate leading to the rather sharp drop-off beyond 0.04 ppp.

### 3.3 Timing template

While an asymmetric timing template is a must for single-frame ME-STB, the temporal separation between exposures can be considered as an additional variable to optimize the design of the template, to maximize the tracking robustness or the dynamic range of the measurement. This is explored for ME(3) sequences by solely increasing the time separation between the second and third exposure. For all cases, the seeding density is set at ppp = 0.01 (cppp = 0.03). The tracking performance is shown in Fig. 7(left) in terms of detection and error rates. As the time separation increases, only a minor decrease of detection rate is observed and the error rate remains below significant levels. These results confirm the adequacy of the chosen trace detectability criteria (Sect. 2.2) as being able to recover correct traces even with a relatively long particle displacement.

The accuracy of the measured velocity is expressed in terms of velocity dynamic range (DVR, Adrian 1997). The DVR is defined as the ratio between the maximum and minimum measurable velocity (more precisely the minimum resolvable velocity fluctuation, $u_{min}'$, see Eq. (9) in Adrian 1997) and computed here by:

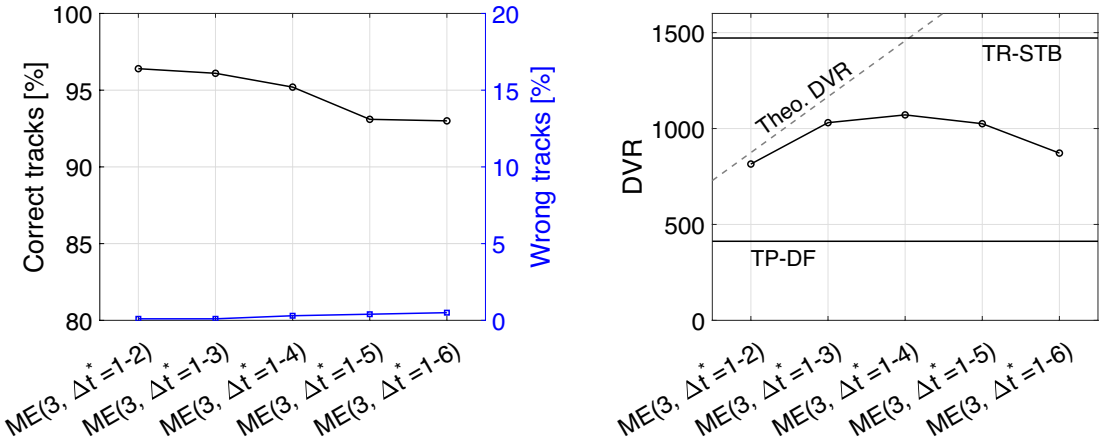


**Fig. 7** Detection rate and erroneous traces as a function of the second time interval (left) and the dynamic velocity range (right)

$$\mathrm{DVR} = \frac{u_{max}}{u_{min}\prime} = \frac{u_0}{\sigma_u} \tag{5}$$

where $u_{min}\prime$ is dictated by the measurement uncertainty $\sigma_u$, which may be decreased when using more exposures, with $u_{max}$ increased for longer traces. Note that a possible inability to measure small velocities due to overlapping particles is not taken into account here, see Appendix for further details.

For a two-pulse double-frame acquisition, the velocity and the uncertainty via error propagation are obtained by:

$$\boldsymbol{u} = \frac{\boldsymbol{x}_2 - \boldsymbol{x}_1}{t_2 - t_1} = \frac{\Delta \boldsymbol{x}_1}{\Delta t_1} \tag{6}$$

$$\sigma_{\boldsymbol{u}} = \frac{\sqrt{2}}{\Delta t_1}\sigma_{\boldsymbol{x}} \tag{7}$$

where it has been assumed that the uncertainty of the particle location, $\sigma_{\boldsymbol{x}}$, follows a Gaussian distribution.

For ME(3), estimating the velocity and uncertainty at the intermediate time using a second-order polynomial leads to:

$$\boldsymbol{u} = \frac{\Delta \boldsymbol{x}_1 + \Delta \boldsymbol{x}_2}{\Delta t_1 + \Delta t_2} \tag{8}$$

$$\sigma_{\boldsymbol{u}} = \frac{2}{\Delta t_1 + \Delta t_2}\sigma_{\boldsymbol{x}}. \tag{9}$$

For the sequence ME(3, $\Delta t^* = 1$–2), the theoretical DVR approximately doubles that of TP-DF. It further increases as the second time separation is elongated, and then, it reduces again, as ascribed to the growth of truncation errors. The DVR obtained for the current analysis is shown in Fig. 7(right), using the rms of the velocity error to estimate the minimum velocity. The values obtained for TR-STB and TP-DF measurements at ppp = 0.01 are also included for reference. A theoretical estimate of the attainable DVR is constructed from Eq. (9), where the positional uncertainty has been extracted from the TP-DF system. For the shorter ME(3) sequences considered, the measured DVR is only slightly below the theoretical estimate due to the increased positional error at the higher ppp of 0.03. Instead, the values start decreasing for the higher temporal separation as a result of the increasing role of truncation errors, which underestimate the curvature of particle paths in the Taylor–Green vortex flow field. Overall, a significant DVR increase can be obtained with respect to TP-DF, despite the higher cppp level, at an intermediate level of that obtained using TR-STB.

### 3.4 Number of pulses

While maintaining the cppp level in the appropriate range (Sect. 3.2), more than three pulses offer the potential to further increase the measurement dynamic range although at lower spatial resolution. A higher number of pulses positively impacts the estimation of velocity based on polynomial regression of the discrete particle samples. Sequences of up to five exposures have been considered, for both single- and double-frame systems. For a single-exposure seeding density of ppp = 0.01, tracking results are given in Fig. 8(left). The percentage of correct tracks decreases slightly when using more pulses as a result of the increased cppp. However, no noticeable increase of the error rate is observed. Figure 8(right) illustrates the error of the material derivative (i.e., Lagrangian acceleration). When normalized, the error is below 2% for TR-STB and about 2% for a double-frame five-pulse measurement. Other options yield

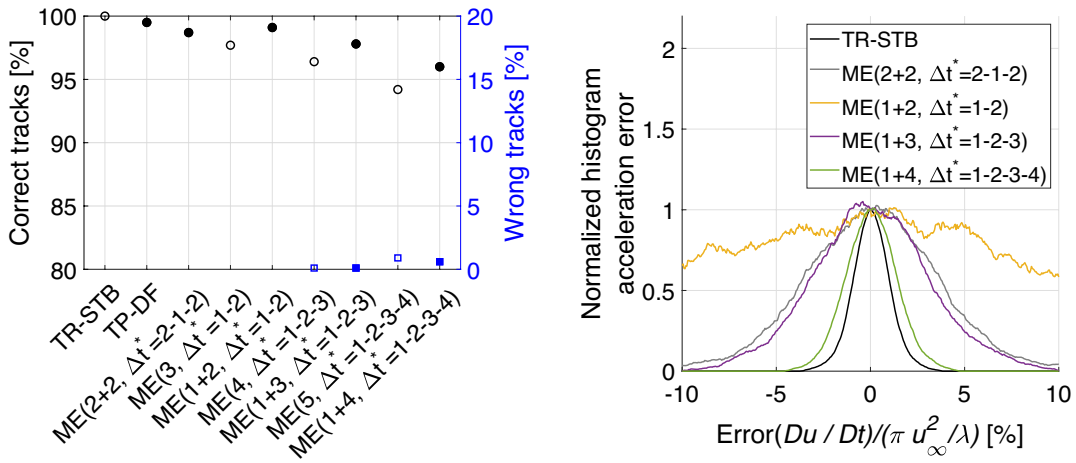


**Fig. 8** Percentage of correct and wrong tracks (left) and normalized histogram of horizontal acceleration error (right), for various timing strategies at ppp = 0.01. Double-frame options are represented by filled symbols

significantly larger errors, with four-pulse methods yielding approximately 4% error irrespective of whether the pulses are equally distributed or not across the two frames. Finally, the three-pulse sequence yields the largest uncertainty exceeding 10%.

Table 1 summarizes the findings from Fig. 8. The accuracies of the velocity and acceleration are expressed in terms of the DVR and dynamic acceleration range (DAR, Schanz et al. 2016), respectively. TR-STB offers the highest accuracy, with DVR of 1500 and DAR exceeding 100. In contrast, the double-frame single-exposure approach yields a DVR of 400. Multi-exposure strategies with three and four pulses clearly outperform TP-DF (DVR ~ 1000), but offer a very modest DAR with three exposures (DAR < 10). The latter improves with the number of exposures, but it remains in the range of 30–60. A five-exposure recording deteriorates the DVR, presumably as a result of higher positional errors (higher cppp) and truncation effects (longer traces). In summary, double-frame options (indicated by filled symbols in Fig. 8(left)), such as the ME(2 + 2, $\Delta t^*$=2–1-2) system, offer optimal performance nearing that of TR-STB and are suited for maximizing seeding density (and therefore the dynamic spatial range, DSR) together with the velocity dynamic range. Regarding the acceleration, the use of more exposures is beneficial as random errors tend to dominate the acceleration uncertainty. This trend is, however, valid only at very low levels of the seeding density (ppp < 0.01) where the additional exposures do not bring cppp at levels where the reconstruction error becomes dominated by ghost particles.

## 4 Experimental verification

### 4.1 Instrumentation and layout

Volumetric measurements of the flow around a wall-mounted cube discussed by Hendriksen et al. (2024) are considered. The experiments, conducted in the W-tunnel facility (low-speed, open jet) at the aerodynamics laboratories of the Aerospace Engineering Department of TU Delft, feature a 12-cm-side-length cube installed on a flat plate immersed in a stream at $u_\infty = 10$ m/s. Submillimeter ($d \sim 0.4$ mm) helium-filled soap bubbles are used as flow tracers, illuminated by two *LED-Flashlight 300* arrays from LaVision GmbH and imaged by seven high-speed cameras (Photron *FastCam*, 1 Mpx, 12-bit) at a rate of 3 kHz. The whole volumetric dataset encompasses a domain of 40 × 40x30 cm$^3$. The cameras are positioned such that their view covers the entire domain of interest from various directions, and the flowfield is reconstructed using the object-aware STB algorithm (Wieneke and Rockstroh 2024). The seeding density in a single-exposure image is approximately ppp = 0.01, and 10,000 particles are tracked on average every frame.

Multi-exposure images are simulated by summing up the intensity of frames selected from the originally recorded time-resolved (single-exposure) sequence. The time separation between light pulses is used as the base separation for ME, with $\Delta t_0 = 0.33$ ms. The traces obtained from TR-STB are used as reference to benchmark the results from the simulated ME recordings. An indication of image quality and seeding concentration is given in Fig. 9(left), where an original single-exposure image is shown, together with the computed multi-exposure images simulating the condition ME(3, $\Delta t^*$=1–2), in Fig. 9(middle), and ME(5, $\Delta t^*$=1–2-3–4), in Fig. 9(right).

### 4.2 Benchmark

The same multi-exposure strategies presented in the synthetic test case (Sect. 3.4) are considered here. Correct traces are those where particles deviate by less than 1 voxel from the reference (i.e., TR-STB analysis). Tracking results are shown in Fig. 10. As expected for the moderate seeding density (ppp ~ 0.01 and cppp < 0.05), excellent detectability is found, with more than 90% correct detection. The error rate is higher, at around 5%, and comparable to that of TP-DF. This can be ascribed to imperfections associated with the experimental conditions. Furthermore, any erroneous measurement in the TR-STB analysis (experimental ground truth) will be considered an additional error.

The measurement obtained with ME-STB is further scrutinized by direct inspection of the time-averaged flow properties (ensemble-averaging of 100 snapshots). The data are reduced on a Cartesian grid collecting the scattered vectors into cubic bins of 24 mm side length with 75% overlap. A second-order polynomial fits the spatial distribution inside the bin, following Agüera et al., (2016). The flow field is displayed at the symmetry plane (Fig. 11) for TR-STB, TP-DF, a double-frame ME sequence (ME(2 + 2, $\Delta t^*$=2–1-2)) and also a single-frame ME sequence, ME(4, $\Delta t^*$=1–2-3). The

**Table 1** DVR and DAR of various ME 3D-PTV strategies at ppp = 0.01

| | TR-STB | TP-DF | ME | ME | ME | ME | ME | ME | ME |
|---|---|---|---|---|---|---|---|---|---|
| Exposures | 1 | 1 + 1 | 2 + 2 | 3 | 1 + 2 | 4 | 1 + 3 | 5 | 1 + 4 |
| $\Delta t^*$ | – | 1 | 2–1-2 | 1–2 | 1–2 | 1–2-3 | 1–2-3 | 1–2-3–4 | 1–2-3–4 |
| DVR | 1500 | 400 | 1300 | 800 | 1100 | 1000 | 1200 | 600 | 650 |
| DAR | 110 | – | 30 | 6 | 8 | 25 | 30 | 60 | 80 |

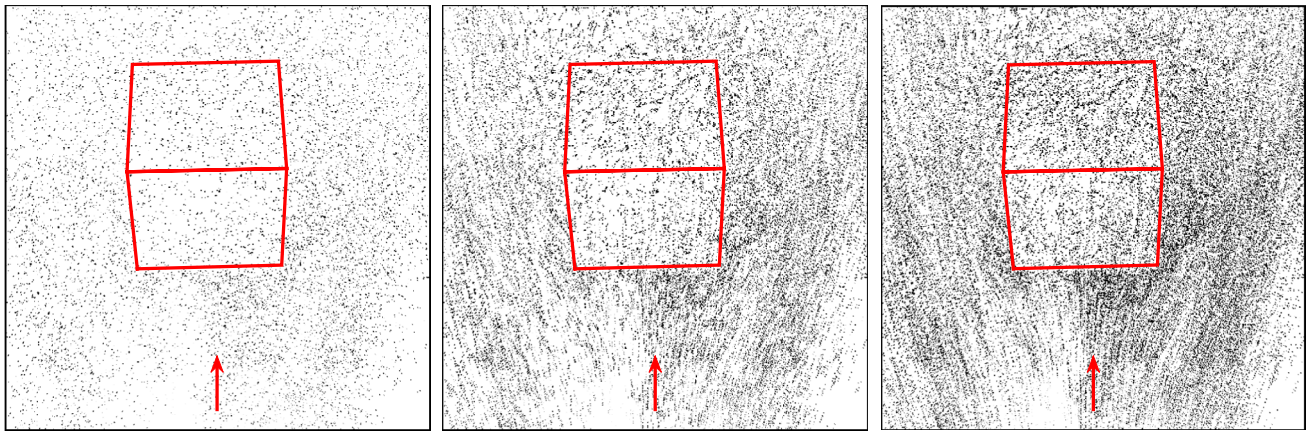

**Fig. 9** Particle images and their sequences around a wall-mounted cube. Left: single-exposure image. Middle: generated multi-exposure, ME(3, $\Delta t^*=1$–2). Right: generated multi-exposure, ME(5, $\Delta t^*=1$–2-3–4)

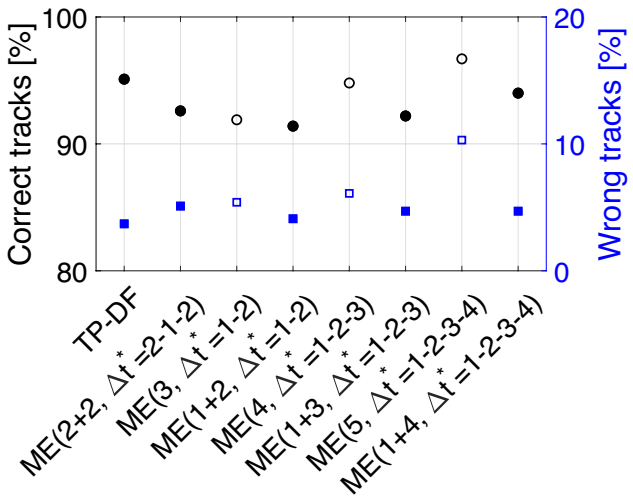


**Fig. 10** Percentage of correct and spurious traces for various 3D-PTV strategies. TR-STB is taken as the reference. Double-frame options are represented by filled symbols

time-averaged streamwise velocity component exhibits no appreciable differences, except for the single-frame ME analysis, differing by some small details.

The map of turbulent fluctuations follows a similar trend, with the single-exposure method being affected by a slight underestimation of peak value at the horseshoe vortex and at the front of the cube. Finally, the material acceleration obtained with ME(2 + 2, $\Delta t^*$=2–1-2) show a remarkable agreement with TR-STB indicating the potential to serve as basis for pressure evaluation. The single-frame ME analysis does capture the acceleration at the leading edge, but again, the details of the horseshoe vortex are not captured, arguably due to particle images overlapping in the low-speed regions, which pose a fundamental limit to the single-frame ME trace detectability (Scarano et al. 2025).

## 5 Demonstration on ME recordings

### 5.1 Experimental setup and measurement conditions

The wake of a cylinder is measured using the volumetric PIV setup discussed in detail by Grille Guerra et al., (2025). A 60 cm long cylinder with a diameter of $D = 6$ cm is installed vertically at the outlet of the W-tunnel facility (Sect. 4.1), immersed in the freestream flow of $u_\infty = 5$ m/s. This results in a diameter-based Reynolds number of $Re_D = 20,000$. Submillimeter helium-filled soap bubbles are used as flow tracers, illuminated by four *LED-Flashlight 300* arrays, providing the pulsed high-speed illumination needed for ME 3D-PTV, and imaged by ten LaVision *Imager LX* cameras (2 MPx, 4.4 µm pitch, 14 bit). The cameras are mounted on two arrays, containing five cameras each, referred to as *antennas* (Hendriksen et al. 2025), that observe the cylinder wake from each side of the wind tunnel. The cameras are equipped with 25 mm focal length objectives and the f-number is set to $f_\#$= 8 in order to achieve the desired depth of field. For the given configuration, this results in a digital image resolution of 4.4 px/mm. A measurement volume of approximately 7 $D(x)$, 5$D(y)$ and 5$D(z)$ is obtained.

At full resolution, the maximum acquisition frequency of the cameras (16 Hz) is insufficient for TR-STB purposes, setting up a relevant condition to justify ME alternatives. Based on the results from previous sections, two ME strategies are explored: ME(2 + 2, $\Delta t^*$=2–1-2) and ME(4, $\Delta t^*$=1–2-3). The smallest time separation between pulses, $\Delta t_0$, is set equal to 0.25 ms, corresponding to a particle displacement of approximately 5 px at the freestream velocity. Raw images from both recordings are shown in Fig. 12. The flow direction and cylinder trailing edge are indicated by a red arrow and line, respectively.

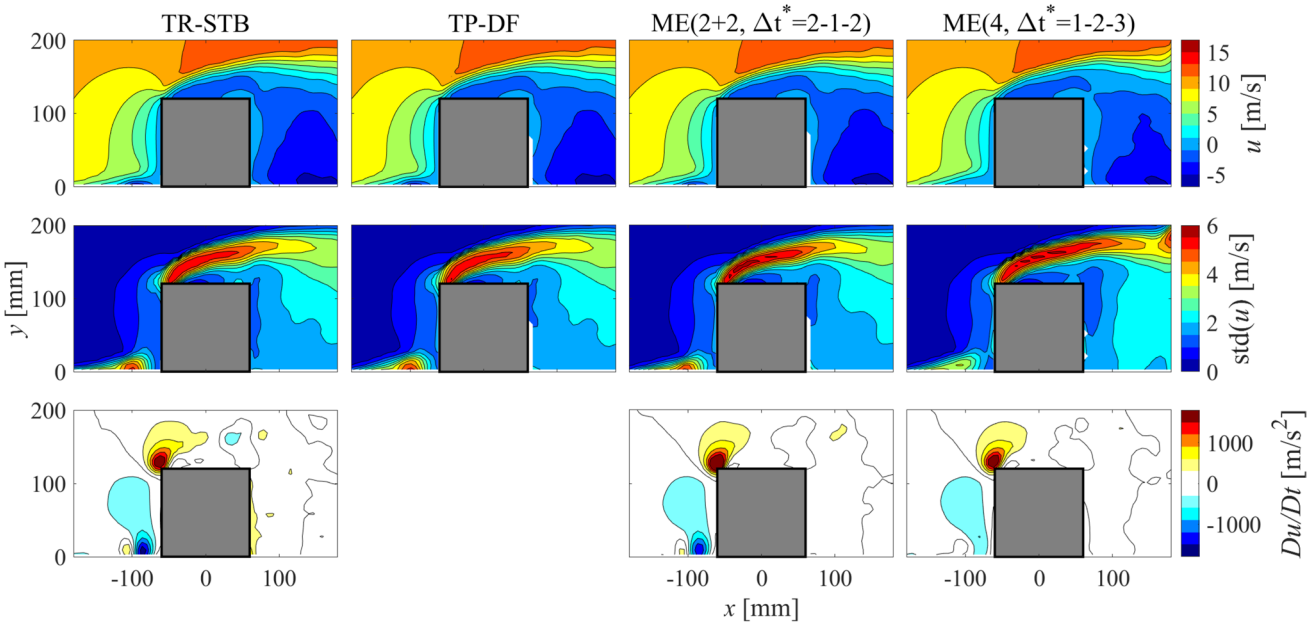


**Fig. 11** Time-averaged streamwise velocity (top), standard deviation of streamwise velocity (middle) and streamwise material acceleration (bottom), for TR-STB, TP-DF, ME(2 + 2, $\Delta t^*$ = 2–1-2) and ME(4, $\Delta t^*$ = 1–2-3)

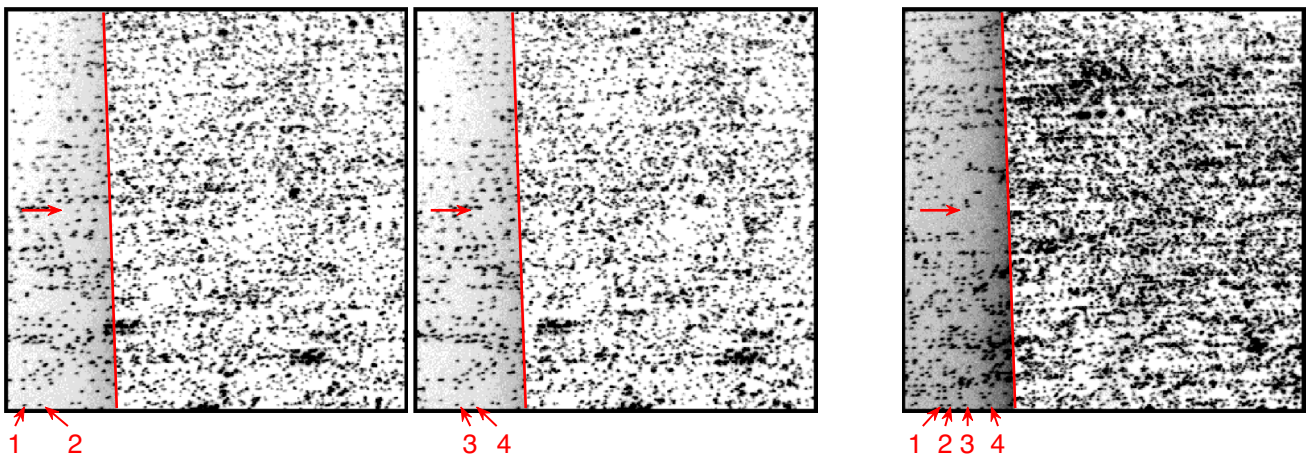


**Fig. 12** ME images of the flow in the wake of a cylinder, with the flow direction and cylinder trailing edge indicated by a red arrow and line, respectively. Left: first frame of an ME(2 + 2, $\Delta t^*$ = 2–1-2) recording. Middle: second frame of a ME(2 + 2, $\Delta t^*$ = 2–1-2) recording. Right: ME(4, $\Delta t^*$ = 1–2-3) recording. The four illumination pulses are indicated for a single tracer in the bottom left region of the images

The timing template is revealed by following a single tracer in the bottom left region of the images, and the illumination pulses are also indicated for further clarity. The baseline seeding density (for a single exposure) is ppp = 0.02. In the double-frame scenario, the cumulative seeding density c ppp ~ 0.04 and it increases to 0.08 when recording onto a single frame.

## 5.2 Velocity and pressure distribution

Approximately 40,000 traces are extracted for each ME recording, corresponding to a particle concentration of approximately 1 particles/cm$^3$. An instantaneous visualization of traces, colored by the associated streamwise velocity is given in Fig. 13. For improved visualization, only a slab of 5 cm in the spanwise direction is depicted. The particle trajectories already reveal the main features of the cylinder wake flow, i.e., the shedding of vortices (Kármán street)

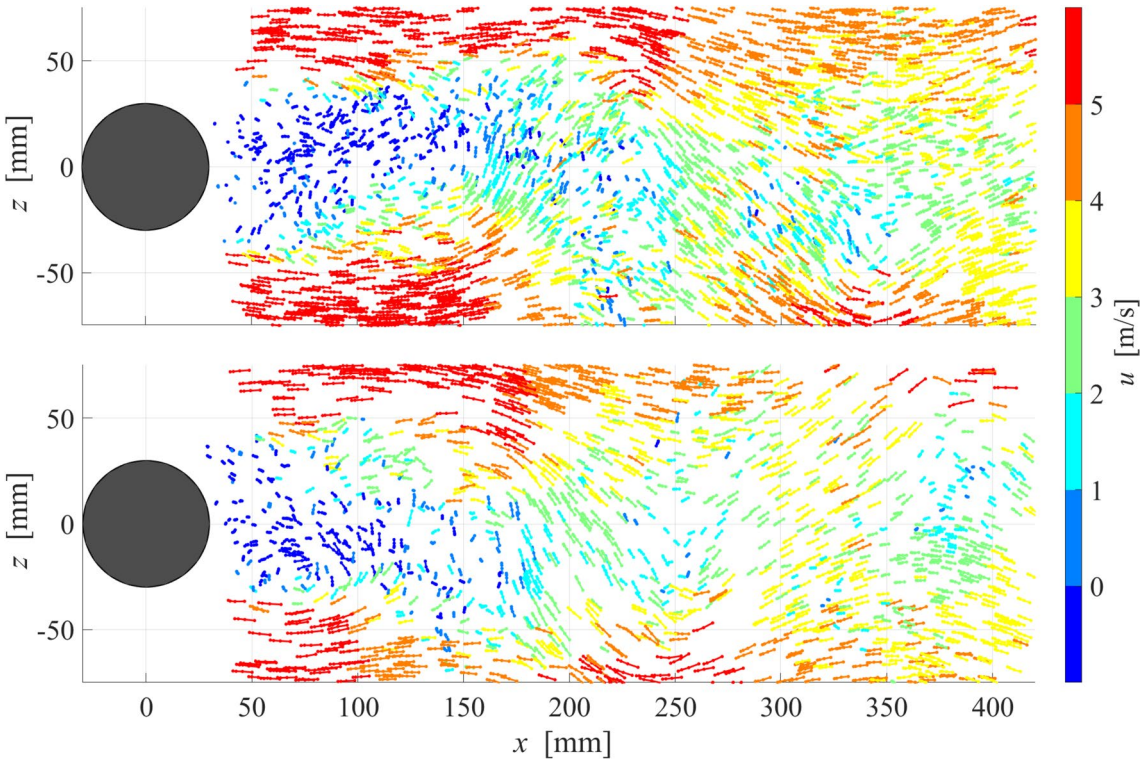


**Fig. 13** Instantaneous visualization of ME traces in the wake of a cylinder, for a slab of 5 cm along the span, and colored by streamwise velocity. Top: belonging to ME(2 + 2, $\Delta t^* = 2$–1-2). Bottom: for ME(4, $\Delta t^* = 1$–2-3)

from the shear layers on both sides of the cylinder. The tracking method proves effective also in the recirculation region close to the back of the cylinder, despite the limited particle displacement.

The availability of acceleration information from the ME traces makes it possible to employ advanced data assimilation schemes to represent the instantaneous flow field on a Cartesian grid. The VIC# method, implemented in the DaVis 11 software (Jeon et al. 2022), has been applied on a grid of 2.5 mm pitch, which corresponds to 64 grid points per trace, following the indications given by Schneiders and Scarano (2016). An instantaneous representation of the three-dimensional flow field is shown in Fig. 14 using isosurfaces of vorticity, color coded by their sign and component.

For both ME recordings, the illustrations reveal the presence of spanwise coherent vortices (Williamson 1996), shed with an alternating sign, visualized through isosurfaces of spanwise vorticity ($\omega_y = \pm 250$ Hz, red and blue, respectively). These main rollers feature an oblique orientation with respect to the cylinder axis (Szepessy and Bearman 1992) and undulations of wavelength larger than the cylinder diameter (Prasad and Williamson 1997). The illustrations also reveal the presence of thinner, streamwise-oriented vortical structures interconnecting the main rollers, as reported in literature for measurements at comparable Reynolds numbers (Grille Guerra et al. 2024; Scarano and Poelma 2009). These structures are visualized through isosurfaces of streamwise vorticity ($\omega_x = \pm 250$ Hz, yellow and green, respectively).

From ME 3D-PTV, not only the velocity–vorticity flow field may be obtained, but also an instantaneous representation of the pressure field thanks to the direct estimation of Lagrangian acceleration. The static pressure is obtained here via solving a Poisson equation (Van Oudheusden 2013) with Neumann boundary conditions. Contours of the static pressure coefficient, $c_p$, at the plane $y = 0$ are shown in Fig. 15 for the two ME sequences explored. As expected, the pressure field is dominated by the low pressure in the core of the main rollers (Fig. 14), thus confirming the suitability of the approach.

## 6 Conclusions

The accuracy of multi-exposure (ME) 3D-PTV has been explored, as a means of increasing the dynamic ranges of volumetric PIV measurements involving low-frame-rate hardware, together with adding information about Lagrangian acceleration and instantaneous pressure. An ME-STB tracking algorithm has been introduced, which can deal with arbitrary timing sequences for both single- and double-frame ME recordings. For single-frame systems, which alleviate

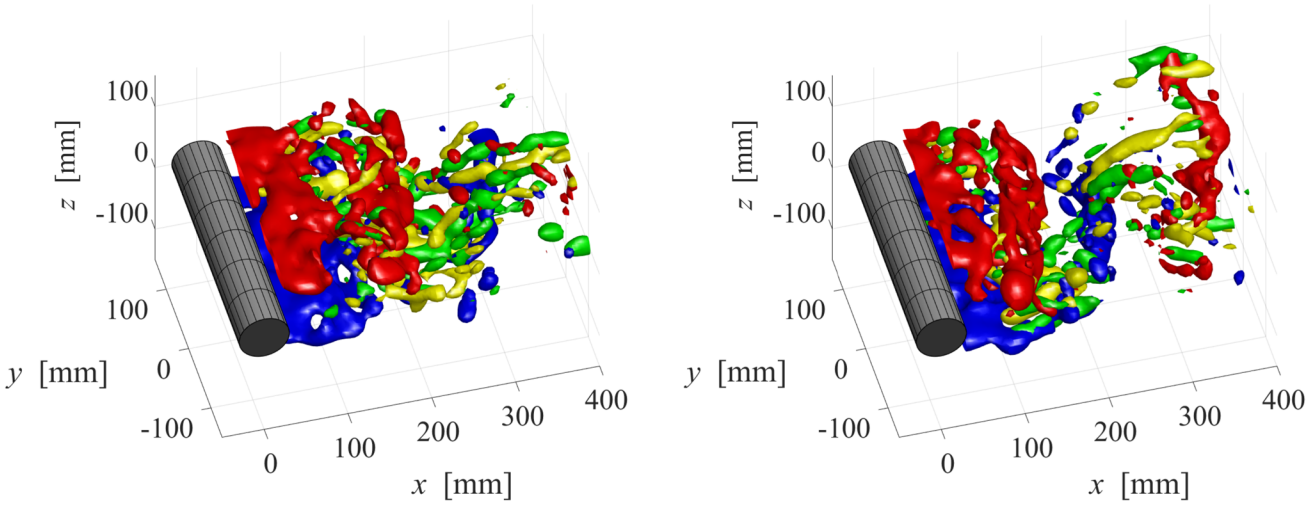


**Fig. 14** Instantaneous visualization of the three-dimensional flow field in the wake of a cylinder using isosurfaces of spanwise ($\omega_y = \pm 250$ Hz, red and blue, respectively) and streamwise ($\omega_x = \pm 250$ Hz, yellow and green, respectively) vorticity. Left: for ME(2 + 2, $\Delta t^* = 2$–1-2). Right: for ME(4, $\Delta t^* = 1$–2-3)

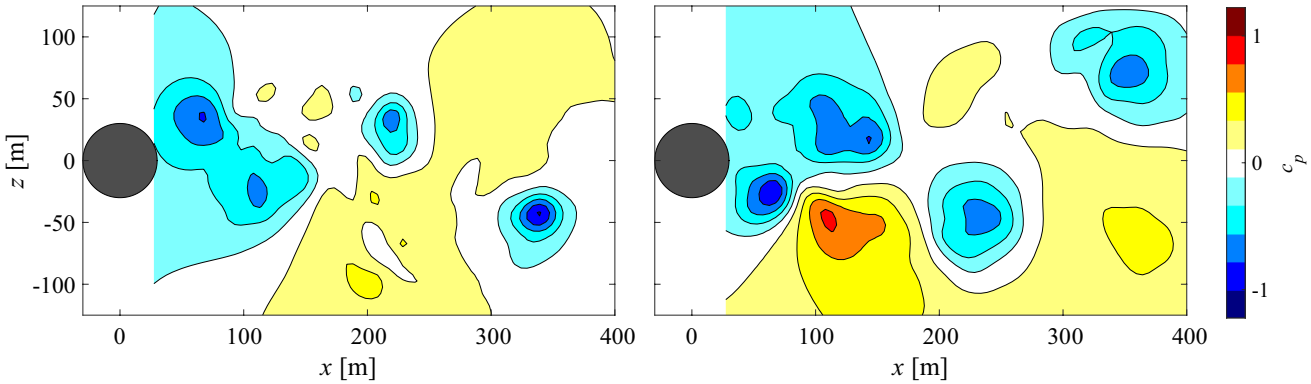


**Fig. 15** Contours of static pressure coefficient, $c_p$, at $y = 0$. Left: for ME(2 + 2, $\Delta t^* = 2$–1-2). Right: for ME(4, $\Delta t^* = 1$–2-3)

the hardware and synchronization requirements, tracking is made possible by making use of asymmetric timing templates (Scarano et al. 2025).

A synthetic test case, based on a Taylor–Green vortex lattice, is initially considered to explore the effects of particle seeding density and timing strategy, which is later complemented using images from an experimental database of the flow around a wall-mounted cube. For both synthetic and experimental images, the proposed ME-STB algorithm shows excellent tracking performance (detection rate above 90%) for cumulative seeding densities below cppp = 0.12, found to be limited by the particle triangulation step. The results appear to be almost independent of the timing template selected and the dynamic velocity range (DVR) doubles that of single-exposure double-frame systems, approaching the values attainable by TR-STB. Besides, acceleration can be accurately estimated when using several exposures, with dynamic acceleration range (DAR) values in the order of 100 for the synthetic test case.

The method is demonstrated using experimental ME images from the flow in the wake of a cylinder, measured using a large-scale volumetric PIV setup (measurement volume of approximately 40 L) involving low-frame-rate cameras and LED modules for pulsed illumination. Around 40,000 particle traces could be extracted every instant for both single- and double-frame ME recordings at a base seeding density of ppp = 0.02. The information from the traces (position, velocity and acceleration) is used to obtain a representation of the three-dimensional flow field on a Cartesian grid of 2.5 mm pitch using the VIC# data assimilation scheme. This allows visualizing not only the spanwise coherent vortices in the wake (Kármán street) but also smaller vortical structures interconnecting the main rollers in the streamwise direction. Finally, the instantaneous pressure

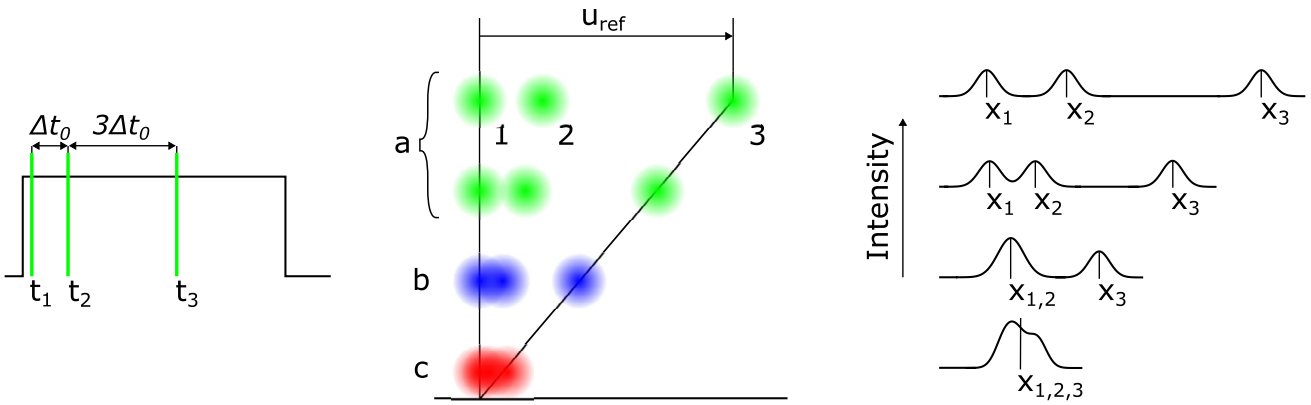


**Fig. 16** Traces generated by a three-pulse sequence (left) for a linear velocity profile (middle). Particle image intensity (right) indicates the appearance of three regimes: (*a*) formation of a *dotted trace*; (*b*) two collapsed dots and a separate one (*streak–dot*); (*c*) all dots are indistinguishable (*streak*)

field could be estimated using the Lagrangian acceleration obtained from the ME traces, highlighting the potential of ME 3D-PTV in this regard.

The main limitation of ME recording strategies remains the difficulty of dealing with low-velocity regions and the associated overlapping particles. This problem can be mitigated employing double-frame timing strategies and modifications to the tracking algorithm to treat these special situations, as recently explored by Scarano et al. (2025).

## Appendix: detection of low-velocity traces

The generation of trace candidates discussed in Sect. 2.1 requires the successful reconstruction of the $N$ particles composing an ME trace. In regions of low velocity, particle images overlap and therefore less than $N$ particles might be reconstructed by the IPR algorithm. This is illustrated in Fig. 16 for a single-frame recording measuring a linear velocity profile. A sequence of three pulses with an asymmetric template is considered, in the shape ME(3, $\Delta t^*$=1–3), as illustrated in Fig. 16(left).

In the portions of the flow with higher velocity (Fig. 16—middle), the multiple exposures produce a trace with spacing analogous to the temporal template of light pulses. Below a certain velocity, the two particle images corresponding to the shortest time separation start to overlap (Fig. 16—right), posing a challenge to the particle reconstruction step. For IPR, the limit condition to detect separate particles is reported to be approximately 50% overlap among particle images. As long as the overlap is below this threshold, all $N$ dots of the trace will be reconstructed (*dotted trace*, or regime *a*, indicated in green in Fig. 16) and no modifications of the candidates generation step are necessary.

For higher overlap, a merged particle will be reconstructed at $\boldsymbol{x}_{1,2} = \frac{\boldsymbol{x}_1+\boldsymbol{x}_2}{2}$, forming a *streak–dot* pattern for the trace (regime *b*, indicated in blue in Fig. 16). This possibility can be accounted for in the trace candidate generation step by allowing traces with less than $N$ entries. The velocity associated with *streak–dot* traces of only two elements suffers from directional ambiguity. However, the first dot (blob) is produced by two overlapping exposures and will feature a higher overall energy and a measurable higher peak intensity (see Fig. 16—right). Similar to the pulse tagging approach (Grant & Liu 1990), the velocity vector can be pointed in the direction from relative high- to low-intensity dots. For a more accurate estimation of the velocity, the time separation between $\boldsymbol{x}_{1,2}$ and $\boldsymbol{x}_3$ is considered to be $\Delta t_1/2+\Delta t_2$, while the acceleration cannot be estimated and is set to zero.

In regions of very low velocity, all particle images composing the trace will merge into a single blob or *streak* (regime *c*, indicated in red in Fig. 16), of skewed intensity for asymmetric timing templates. In this regime, no velocity can be extracted directly from single-frame recordings. However, the trace might be continued in the subsequent frame of the recording given the low velocity, as recently explored by Scarano et al. (2025). This interframe analysis to tackle regime *c* has not been considered in the present work and is subject to further research.

For double-frame recordings, the situation is simpler and restricted to the analysis of regimes *a* and *b* only, where, for example, for ME(2 + 2, $\Delta t^*$=2–1-2), regime *b* corresponds to streaks in both frames, which can nevertheless be processed down to zero veclocities.

The proposed approach is explored for the synthetic test case already introduced in Sect. 3, but now imposing a zero out-of-plane velocity component ($w = 0$) to introduce regions of low velocity in the domain. A single-frame recording, ME(3, $\Delta t^*$=1–3), at a base seeding density of ppp = 0.01 is considered. Particles reconstructed by IPR

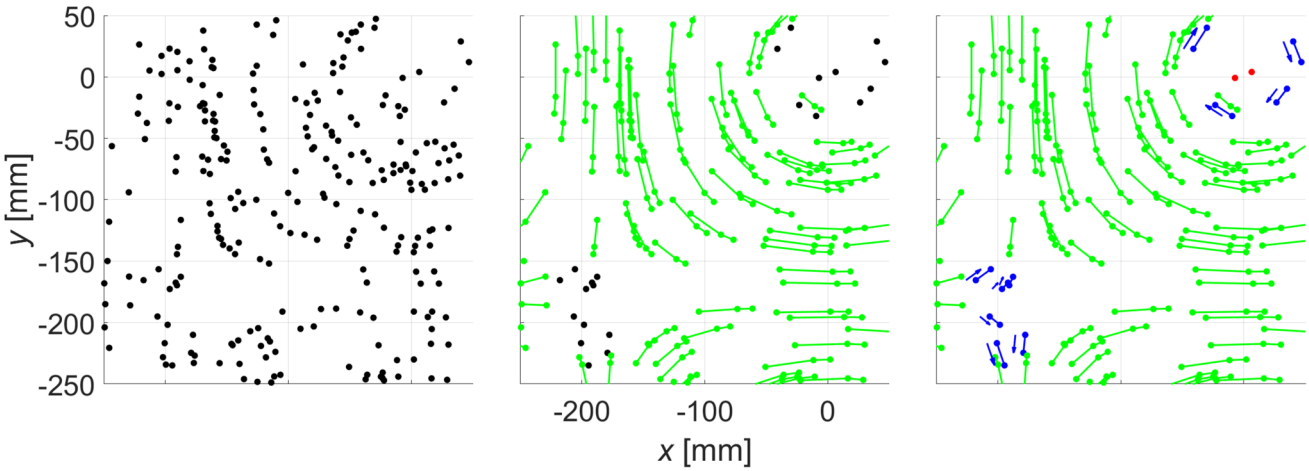


**Fig. 17** Reconstructed particles (left), detected traces in the *dotted-trace* regime only (middle) and including the *streak–dot* regime (right) for a single-frame recording, ME(3, $\Delta t^*$ = 1–3), at ppp = 0.01

are shown in Fig. 17(left) in a subdomain described by the dashed black square in Fig. 5(left).

Without accounting for possible traces outside the *dotted-trace* regime (regime *a* in Fig. 16), the detected traces are the ones shown in Fig. 17(middle), each composed of three distinct particle images. It can be seen that some particles are left unmatched in regions of low velocity, i.e., the vortex core and saddle point. In this situation, the minimum measurable velocity is dictated by the minimum separation between particles, and a region spatial void of particles is introduced that reflects the velocity range gap. If particles cannot be detected separately at a distance below 1 px distance (2 px particle image diameter, see Sect. 3.1), the ratio of maximum to minimum measurable velocity would drastically decrease to $\frac{u_{max}}{u_{min}} = \frac{5}{1} = 5$. Allowing for traces in the *streak–dot* regime (regime *b* in Fig. 16) makes it possible to recover traces composed of two dots only (Fig. 17—right, indicated in blue). In this case, however, the ambiguity of flow direction needs to be solved by other approaches. Potential approaches, which remain to be investigated and proved viable are: 1) spatial regularity of the velocity vector direction; 2) intensity distribution across the dots. The first approach is viable when a sufficient number of dotted traces is found in the surrounding of the streak–dot. The second is generally viable as long as the particle image detector yields a reliable estimate of the dot intensity. Finally, for these traces, no information on acceleration can be extracted. The minimum measurable velocity now occurs when all dots merge, this is, $\frac{u_{max}}{u_{min}} = \frac{5}{1/3} = 15$. In general, the measurement gap may be minimized by increasing the time separation between the final light pulses (e.g., using ME(3, $\Delta t^*$=1–6)), which is found to have a minor effect on the tracking performance, as discussed in Sect. 3.3. Still, a few particles very close to the vortex core (indicated in red), belonging to the *streak* regime (regime *c* in Fig. 16), cannot be tracked with the current algorithm.

Apart from introducing a measurement gap, overlapping particles may decrease the DVR of the measurement due to the increased uncertainty in the particle position determination. For double-frame recordings, the attainable DVR in the presence of low-velocity traces can be better estimated since only regimes *a* and *b* need to be tackled. For an ME(2 + 2, $\Delta t^*$=2–1-2) sequence, the rms of the velocity error of traces belonging only to regime *a* produces a DVR of 1300, in agreement with the value reported in Table 1 for the same sequence and no low-velocity traces involved. Instead, the analysis of traces belonging only to regime *b* returns a DVR of approximately 200. This value is roughly one half of that obtained for double-frame single exposure, which is attributed to the increased positional uncertainty of overlapping particles.

**Acknowledgements** The experimental verification database has been made available from an experiment conducted by Luuk Hendriksen, who is kindly acknowledged.

**Author contribution** All authors contributed to the conceptualization of the research. A.G.G conducted the experiments, prepared the figures and wrote the initial draft of the manuscript. All authors reviewed the manuscript.

**Data availability** A digital version of the figures presented in this publication is openly available in the 4TU.ResearchData repository, with https://doi.org/10.4121/487b6596-63f3-4957-9091-7bd17d30ad8a

## Declarations

**Conflict of interests** The authors declare no competing interests.

## References

Adrian RJ (1997) Dynamic ranges of velocity and spatial resolution of particle image velocimetry. Meas Sci Technol 8(12):1393–1398. https://doi.org/10.1088/0957-0233/8/12/003

Adrian RJ, & Westerweel J (2011) *Particle Image Velocimetry*. Cambridge University Press. https://books.google.nl/books?id=jbDl2-yHbooC

Agüera N, Cafiero G, Astarita T, Discetti S (2016) Ensemble 3D PTV for high resolution turbulent statistics. Meas Sci Technol 27(12):124011. https://doi.org/10.1088/0957-0233/27/12/124011

Agüí JC, Jiménez J (1987) On the performance of particle tracking. J Fluid Mech 185(5):447–468. https://doi.org/10.1017/S0022112087003252

Beresh S, Kearney S, Wagner J, Guildenbecher D, Henfling J, Spillers R, Pruett B, Jiang N, Slipchenko M, Mance J, Roy S (2015) Pulse-burst PIV in a high-speed wind tunnel. Meas Sci Technol 26(9):095305. https://doi.org/10.1088/0957-0233/26/9/095305

Boillot A, Prasad AK (1996) Optimization procedure for pulse separation in cross-correlation PIV. Exp Fluids 21(2):87–93. https://doi.org/10.1007/BF00193911

Elsinga GE, Scarano F, Wieneke B, Van Oudheusden BW (2006) Tomographic particle image velocimetry. Exp Fluids 41(6):933–947. https://doi.org/10.1007/s00348-006-0212-z

Godbersen P, Gesemann S, Schanz D, & Schröder A (2024) FlowFit3: Efficient Data Assimilation Of LPT Measurements. In: *Proceedings of the International Symposium on the Application of Laser and Imaging Techniques to Fluid Mechanics*, *21*(1), 1–14. https://doi.org/10.55037/lxlaser.21st.216

Grant I, Liu A (1990) Directional ambiguity resolution in particle image velocimetry by pulse tagging. Exp Fluids 10(2–3):71–76. https://doi.org/10.1007/BF00215013

Grille Guerra A, Sciacchitano A, Scarano F (2024) Iterative modal reconstruction for sparse particle tracking data. Phys Fluids 36(7):0209527. https://doi.org/10.1063/5.0209527

Grille Guerra A, Porcar Galan L, Sciacchitano A, Scarano F (2025) Treatment of light reflections in 3D PIV systems. Meas Sci Technol 36(11):115301. https://doi.org/10.1088/1361-6501/ae1993

Hendriksen LA, Sciacchitano A, Scarano F (2024) Object registration techniques for 3D particle tracking. Meas Sci Technol 35(12):ad715c. https://doi.org/10.1088/1361-6501/ad715c

Hendriksen LA, Grille Guerra A, Sciacchitano A, & Scarano F (2025) Omnidirectional Particle Image Velocimetry. In: *Proceedings of the 16th International Symposium on Particle Image Velocimetry*.

Hysa I, Tuinstra M, Sciacchitano A, Scarano F, van der Meulen MJ, Rockstroh T, Roosenboom EWM (2024) A multi-directional redundant 3D-LPT system for ship–flight–deck wind interactions. Exp Fluids 65(8):1–15. https://doi.org/10.1007/s00348-024-03867-0

Jahn T, Schanz D, Schröder A (2021) Advanced iterative particle reconstruction for Lagrangian particle tracking. Exp Fluids 62(8):1–24. https://doi.org/10.1007/s00348-021-03276-7

Jeon YJ, Müller M, Michaelis D (2022) Fine scale reconstruction (VIC#) by implementing additional constraints and coarse-grid approximation into VIC+. Exp Fluids 63(4):70. https://doi.org/10.1007/s00348-022-03422-9

Kähler CJ, Astarita T, Vlachos PP, Sakakibara J, Hain R, Discetti S, La Foy R, Cierpka C (2016) Main results of the 4th International PIV Challenge. Exp Fluids 57(6):1–71. https://doi.org/10.1007/s00348-016-2173-1

Le Bris J, Leclaire B, Cornic P, Champagnat F, Musci B, Cheminet A (2025) Consensus-based tracking for 3D PTV at high seeding densities. Exp Fluids 66(10):1–24. https://doi.org/10.1007/s00348-025-04109-7

Maas HG, Gruen A, Papantoniou D (1993) Particle tracking velocimetry in three-dimensional flows - Part 1. Photogrammetric determination of particle coordinates. Exp Fluids 15(2):133–146. https://doi.org/10.1007/BF00190953

Malik NA, Dracos T, Papantoniou DA (1993) Particle tracking velocimetry in three-dimensional flows - Part II: Particle tracking. Exp Fluids 15(4–5):279–294. https://doi.org/10.1007/BF00223406

Nishino K, Kasagi N, Hirata M (1989) Three-dimensional particle tracking velocimetry based on automated digital image processing. J Fluids Eng 111(4):384–391. https://doi.org/10.1115/1.3243657

Novara M, Schanz D, Reuther N, Kähler CJ, Schröder A (2016) Lagrangian 3D particle tracking in high-speed flows: Shake-The-Box for multi-pulse systems. Exp Fluids 57(8):1–20. https://doi.org/10.1007/s00348-016-2216-7

Novara M, Schanz D, Geisler R, Gesemann S, Voss C, Schröder A (2019) Multi-exposed recordings for 3D Lagrangian particle tracking with Multi-Pulse Shake-The-Box. Exp Fluids 60(3):1–19. https://doi.org/10.1007/s00348-019-2692-7

Novara M, Schanz D, Schröder A (2023) Two-pulse 3D particle tracking with Shake-The-Box. Exp Fluids 64(5):1–21. https://doi.org/10.1007/s00348-023-03634-7

Prasad A, Williamson CHK (1997) Three-dimensional effects in turbulent bluff-body wakes. J Fluid Mech 343:235–265. https://doi.org/10.1017/S002211209700579X

Saredi E, Sciacchitano A, Scarano F (2020) Multi-Δt 3D-PTV based on Reynolds decomposition. Meas Sci Technol 31(8):084005. https://doi.org/10.1088/1361-6501/ab803d

Scarano F, Poelma C (2009) Three-dimensional vorticity patterns of cylinder wakes. Exp Fluids 47(1):69–83. https://doi.org/10.1007/s00348-009-0629-2

Scarano F, Hysa I, Grille Guerra A, Tuinstra M, Sciacchitano A (2025) Asymmetric time sequence for multiple-exposure 3D PTV. Exp Fluids 66(4):74. https://doi.org/10.1007/s00348-025-03993-3

Scarano F, Grille Guerra A, & Wieneke B (2025) Detection of low-velocity traces in ME-PTV. In: *Proceedings of the 16th International Symposium on Particle Image Velocimetry*.

Schanz D, Gesemann S, Schröder A (2016) Shake-the-Box: Lagrangian particle tracking at high particle image densities. Exp Fluids. https://doi.org/10.1007/s00348-016-2157-1

Schneiders JFG, Scarano F (2016) Dense velocity reconstruction from tomographic PTV with material derivatives. Exp Fluids 57(9):1–22. https://doi.org/10.1007/s00348-016-2225-6

Schröder A, Schanz D (2023) 3D Lagrangian particle tracking in fluid mechanics. Annu Rev Fluid Mech 55(1):511–540. https://doi.org/10.1146/annurev-fluid-031822-041721

Szepessy S, Bearman PW (1992) Aspect ratio and end plate effects on vortex shedding from a circular cylinder. J Fluid Mech 234(1):191. https://doi.org/10.1017/S0022112092000752

Thurow B, Jiang N, Lempert W (2013) Review of ultra-high repetition rate laser diagnostics for fluid dynamic measurements. Meas Sci Technol. https://doi.org/10.1088/0957-0233/24/1/012002

Van Oudheusden BW (2013) PIV-based pressure measurement. Meas Sci Technol. https://doi.org/10.1088/0957-0233/24/3/032001

Wieneke B (2013) Iterative reconstruction of volumetric particle distribution. Meas Sci Technol. https://doi.org/10.1088/0957-0233/24/2/024008

Wieneke B, Rockstroh T (2024) Lagrangian particle tracking in the presence of obstructing objects. Meas Sci Technol 35(5):055303. https://doi.org/10.1088/1361-6501/ad289d

Williamson CHK (1996) Vortex dynamics in the cylinder wake. Annu Rev Fluid Mech 28:477–539. https://doi.org/10.1146/annurev.fl.28.010196.002401

Willneff J (2003) *A Spatio-Temporal Matching Algorithm for 3D Particle Tracking Velocimetry*. ETH Zurich.

Zhang D, Tropea C, Zhou W, Cai T, Huang H, Dong X, Gao L, Cai X (2024) Particle streak velocimetry: a review. Exp Fluids. https://doi.org/10.1007/s00348-024-03857-2